ACS NANO

www.acsnano.org

Low-Temperature Activation and Coupling of Methane on MgO Nanostructures Embedded in $Cu_2O/Cu(111)$

Arephin Islam, Erwei Huang, Yi Tian, Pedro J. Ramírez, Kasala Prabhakar Reddy, Hojoon Lim, Nathaniel White, Adrian Hunt, Iradwikanari Waluyo, Ping Liu, and José A. Rodriguez*

Cite This: *ACS Nano* 2024, 18, 28371−28381

Read Online

ACCESS | Metrics & More | Article Recommendations | Supporting Information

ABSTRACT: **The efficient conversion of methane into valuable hydrocarbons, such as ethane and ethylene, at relatively low temperatures without deactivation issues is crucial for advancing sustainable energy solutions. Herein, AP-XPS and STM studies show that MgO nanostructures (0.2−0.5 nm wide, 0.4−0.6 Å high) embedded in a $Cu_2O/Cu(111)$ substrate activate methane at room temperature, mainly dissociating it into CH_x ($x = 2$ or 3) and H adatoms, with minimal conversion to C adatoms. These MgO nanostructures in contact with $Cu_2O/Cu(111)$ enable C−C coupling into ethane and ethylene at 500 K, a significantly lower temperature than that required for bulk MgO catalysts (>700 K), with negligible carbon deposition and no deactivation. DFT calculations corroborate these experimental findings. The $CH_{4,gas} \rightarrow {}^*CH_3 + {}^*H$ reaction is a downhill process on $MgO/Cu_2O/Cu(111)$ surfaces. The activation of methane is facilitated by electron transfer from copper to MgO and the existence of Mg and O atoms with a low coordination number in the oxide nanostructures. The formation of $O-CH_3$ and O−H bonds overcomes the energy necessary for the cleavage of a C−H bond in methane. DFT studies reveal that smaller Mg_2O_2 model clusters provide stronger binding and lower activation barriers for C−H dissociation in CH_4, while larger Mg_3O_3 clusters promote C−C coupling due to weaker ${}^*CH_3$ binding. All of these results emphasize the importance of size when optimizing the catalytic performance of MgO nanostructures in the selective conversion of methane.**

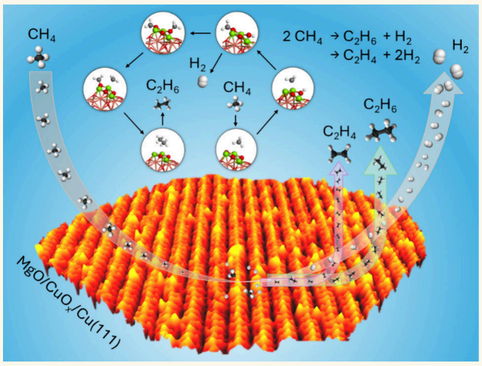

KEYWORDS: *Magnesium oxide nanostructures, Methane activation, Methane coupling, Ethane formation, Ethylene formation*

INTRODUCTION

Natural gas, primarily composed of methane, stands out as a versatile energy resource that has garnered considerable attention from researchers since the 1950s.[1−3] Nowadays, this interest stems from the urgent need to identify greener fuel alternatives capable of replacing conventional petroleum-based fuels. Methane's high hydrogen-to-carbon ratio (4:1) makes it ideal for hydrogen or syngas production through reforming or partial oxidation reactions, offering the potential for reduced carbon dioxide emissions.[3−5] Other approaches demonstrated that methane can be transformed directly into oxygenates, low alkanes, or olefins.[1−3] All of these approaches will require catalytic activation of the molecule at temperatures below 500 K to prevent the decomposition of CH_x fragments that can be used in the production of high-value chemicals.[1,3,4] There is a continuous search for materials that can achieve methane activation at moderate temperatures.[1,2,6]

Bulk MgO is not really active for methane activation or conversion.[7−9] The oxide must be activated by the addition of alkali or late transition metals.[4,7,8] Catalysts combining MgO and nonexpensive metals (Co, Ni, Cu) display a good activity for dry reforming ($CH_4 + CO_2 \rightarrow 2CO + 2H_2$, $\Delta H_0 = +247$ kJ mol^{-1}).[4,5,8] Li-doped MgO is useful for the conversion of methane to ethane or ethylene.[9−11] It can be a direct conversion ($CH_4 \rightarrow 0.5\ C_2H_6 + 0.5\ H_2$, $\Delta H_0 = +33$ kJ mol^{-1} ; $CH_4 \rightarrow 0.5\ C_2H_4 + H_2$, $\Delta H_0 = +101$ kJ mol^{-1}), or it can be facilitated by oxidative coupling ($CH_4 + 0.25O_2 \rightarrow 0.5C_2H_6 + 0.5H_2O$, $\Delta H_0 = -88$ kJ mol^{-1}; $CH_4 + 0.5O_2 \rightarrow 0.5C_2H_4 + H_2O$, $\Delta H_0 = -142$ kJ mol^{-1}). Again, the main bottleneck is in the dissociation of methane on bulk magnesium oxide.[9] Theoretical calculations predict an energy

Received: August 7, 2024
Revised: September 18, 2024
Accepted: September 20, 2024
Published: October 3, 2024

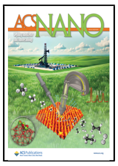

https://doi.org/10.1021/acsnano.4c10811
ACS Nano 2024, 18, 28371−28381

barrier of ∼460 kJ/mol for the dissociation of the first C−H bond of methane on MgO(100).[9] This implies that all the above cited chemical transformations will have to be carried out at temperatures much higher than 500 K, making the survival and transformation of CH_x groups into high-value chemicals extremely difficult.[1−3] Since MgO is a nonexpensive and very common material, it is worthwhile to explore different ways to enhance its reactivity toward methane.

Inverse oxide/metal catalysts where MgO is deposited on the surface of late transition metals offer interesting opportunities that deserve to be tested.[12−16] The catalytic properties of supported MgO films are influenced by metal-to-oxide electron transfer.[14,16] This transfer enhances chemical activity, particularly at the corner or edge atoms in the oxide phase.[14,16−18] A recent theoretical study predicts that the integration of MgO nanostructures with copper oxide (CuO_x) on copper surfaces is a promising strategy for methane activation.[18] This approach offers synergistic effects, combining the high activity of MgO nanostructures[17] with the excellent conductivity of Cu surfaces.[14−16] Notably, Cu-based catalysts have been shown to selectively activate methane and promote its conversion into methanol, a valuable chemical feedstock, at relatively low temperatures.[19−21]

This study uses a combination of synchrotron-based ambient-pressure X-ray photoelectron spectroscopy (AP-XPS), scanning tunneling microscopy (STM), catalytic batch reactor tests, and calculations based on density-functional theory (DFT) to investigate the activation of methane on $MgO/CuO_x/Cu(111)$ surfaces at room temperature and the subsequent transformation of CH_x fragments into C_2H_6, C_2H_4 and H_2. Indeed, nanostructures of MgO dispersed on Cu(111) can catalyze the nonoxidative coupling process of methane at moderate temperatures (500 K). Our findings provide a valid approach for the development of efficient technical catalysts for methane conversion.

RESULTS AND DISCUSSION

MgO Nanocluster on $Cu_2O/Cu(111)$: XPS and STM Analysis. XPS and STM techniques were utilized to examine the growth of MgO nanostructures on $Cu_2O/Cu(111)$ surfaces. On purpose, following the results of previous theoretical studies,[18] small quantities (<0.15 ML) of Mg metal were vapor-deposited onto a single-layer $Cu_2O/Cu(111)$ substrate, which was prepared by preoxidizing Cu(111) with 1×10^{-6} Torr of O_2 at 500 K for 15 min, followed by cooling to room temperature under the same oxygen background.[17] The corresponding O 1s XPS spectrum at the bottom of Figure 1 shows two components at binding energies of 529.8 and 529.3 eV, attributed to lattice (O_L) and non-lattice (O_{NL}) oxygen atoms within a defective $Cu_2O(111)$ film.[17,22−24] This film was less than two monolayers thick, and the bulk of the copper crystal remained in a metallic state (Figure S1).

Mg was vapor deposited on the $Cu_2O/Cu(111)$ substrate at 300 K, and the resulting system was oxidized at 500 K under an atmosphere of O_2. Figure 1 shows the corresponding XPS measurements for the O 1s and Mg 2p XPS regions. The deposition of Mg coverages ranging from 0.036 to 0.11 ML induced oxygen transfer ($Mg + Cu_2O \rightarrow MgO + CuO_x$) from the $Cu_2O/Cu(111)$ substrate to the deposited metal, leading to the formation of MgO and CuO_x. In the O 1s region, decreases in the peaks at 529.3 and 529.8 eV, corresponding to O atoms bound to copper, were observed, along with new peaks for MgO appearing at 531.4 eV, matching previously reported values for MgO clusters and falling within the range of O 1s binding energies for MgO films.[9,17,25,26] In the final oxidation step, the intensity of the peaks for copper-bound O clearly increased with relatively minor changes in the photoemission features associated with MgO. Although the amount of copper-bound O increased on the surface, the bulk of the copper crystal remained in a metallic state (Figures S1−S3).

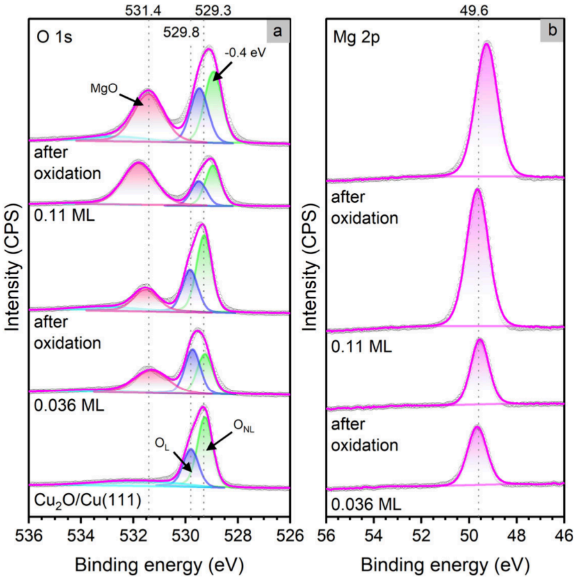

Figure 1. O 1s (a) and Mg 2p (b) XPS spectra for Cu_2O/Cu (111) and $Mg/Cu_xO/Cu(111)$ surfaces with 0.036 and 0.11 ML of Mg. In the O 1s spectrum for Cu_2O/Cu, features for lattice (L) and non-lattice (NL) oxygen atoms in a defective $Cu_2O(111)$ surface are seen. The Mg was vapor-deposited at 300 K, and the sample was exposed to O_2 (1×10^{-6} Torr) at 500 K for 15 min.

STM was used to gain insight into the surface morphological changes associated with the XPS experiments. Figure 2 displays the structure of a freshly prepared $Cu_2O/Cu(111)$ surface.[27,28] It exhibits an atomically flat domain of copper oxide, known as the "29" structure,[17,29,30] with a height of approximately ∼18 pm (Figure 2g: line profile 1) spread across large terraces. Deposition of Mg atoms on this substrate at coverages ranging from 0.036 to 0.11 ML induces oxygen transfer ($Mg + Cu_2O \rightarrow MgO + CuO_x$) from the $Cu_2O/Cu(111)$ substrate to the deposited admetal, leading to the formation of MgO and CuO_x (Figure 1). A disruption in the structure of the copper oxide film by Mg is depicted in Figures 2c and 2d. One can see dark depressions (inside blue dotted circles) coupled with bright spots (inside green dotted circles), reflecting the removal of O by Mg. The bright spots also indicate that there are no preferential landing sites for the Mg on the copper oxide film. The high thermochemical stability of MgO relative to that of copper oxides facilitates instant oxygen removal. Introducing O_2 to the sample at 750 K results in the healing of the copper oxide film, forming a well-ordered film with small clusters (Figure 2g line profile 4: ∼0.35 nm in width, 13 pm in height) of embedded MgO clusters, some of which are incorporated into the hexagonal holes on top of the rows (Figure 2f: inside green dotted circle) or in between them.[28,29] These results are consistent with the increase of the intensity of the O 1s peak at 529.3 and 529.8 eV after oxidation (Figure 1a) and with the existence of sites where one to three atoms of Mg are embedded in the copper oxide film (Figure S4), producing

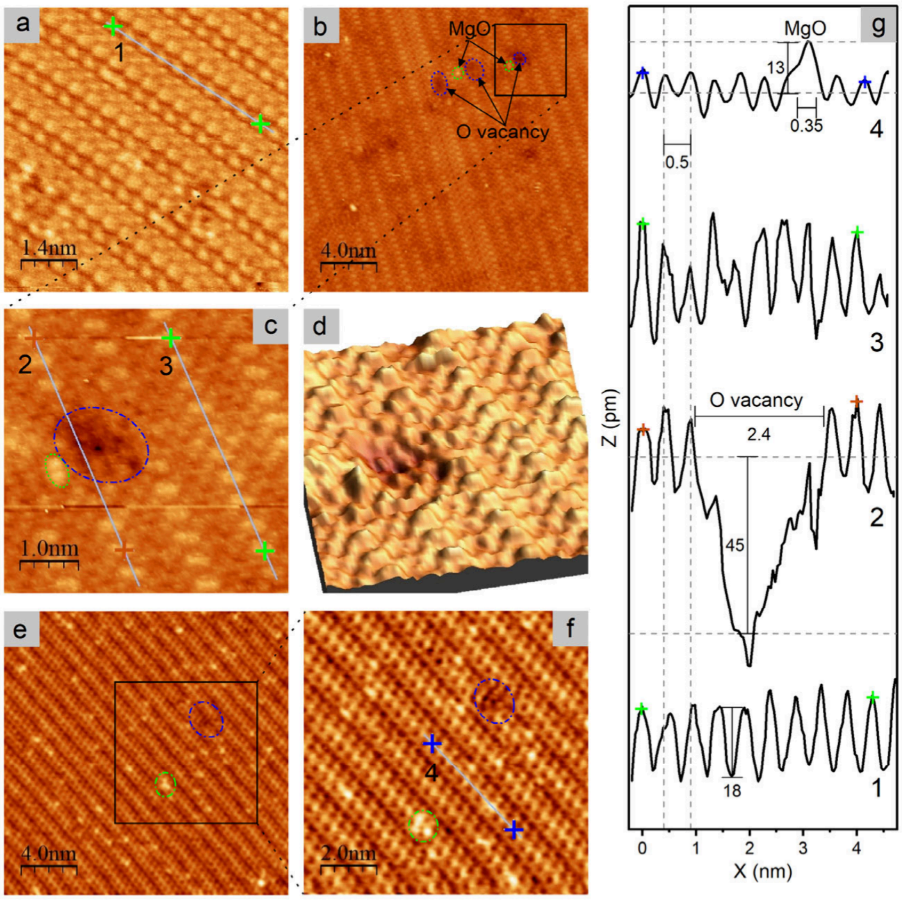

Figure 2. STM images for plain $Cu_2O/Cu(111)$ (a) and a 0.04 ML $MgO/CuO_x/Cu(111)$ surface (b−f). $Cu_2O/Cu(111)$ was prepared by exposing the pristine Cu(111) surface to O_2 (5×10^{-7} Torr) at 750 K for 20 min (a), and Mg was deposited on top of the surface at 300 K (b, c). (d) 3D representation of part c. In the final step, the $Mg/CuO_x/Cu(111)$ surface was exposed to O_2 (5×10^{-7} Torr) at 750 K (e, f). (g) Line profiles over various regions on a, c, and f. Imaging parameters: $I_t = -0.13$ nA, and $V_s = -0.6$ V.

Mg−O units where both atoms have a low coordination number. In Figure 2e,f, there is no disruption in the "29" structure characteristic of the copper oxide film.

At a coverage of 0.11 ML, the O 1s peak in Figure 1a displays a slight shift toward lower (−0.4 eV) binding energy, attributed to increased surface MgO coverage. In Figure 1b, a Mg 2p peak at approximately 49.6 eV is observed, indicative of MgO[9,30,31] presence atop a $CuO_x/Cu(111)$ substrate. This coverage level also induces a minor shift toward lower binding energy in the Mg 2p peak, reflecting the expected mixture of metallic Mg and MgO. Panels a and b in Figure 3 show images of a $Cu_2O/Cu(111)$ surface after depositing 0.1 ML of Mg at 300 K. Relatively big aggregates of MgO coexist with small clusters of the oxide (Figure 3g). Upon oxidation of the system at 500 K, the MgO gets incorporated into rows of copper oxide (3Figure 3c−g). Bright spots come from the MgO nanostructures and parts of the copper oxide film, and they can be separated by their height (see Figure 3d and corresponding line profiles 3 and 4 in Figure 3g). In general, the sizes of the MgO nanostructures are 0.4−0.5 nm in width and 20−70 pm in height. As in the case of the low coverage of 0.04 ML seen in Figure 2, clusters of one to three atoms of Mg (Figure S4) are mixed with the copper oxide. Most of the MgO units are within the copper oxide rows, but some of them are between (Figure 3f). At this MgO coverage of 0.11 ML, some disruption is seen in Figure 3e,f for the "29" structure characteristic of the copper oxide film. Thus, the initial loss of order seen in Figure 3b upon Mg deposition is removed by the dosing of O_2, but the final copper oxide layer is not exactly a pristine $Cu_2O/Cu(111)$ substrate.

It is important to mention that at higher coverages of magnesium (>0.15 ML), the MgO forms on the $CuO_x/Cu(111)$ substrate two-dimensional (2D) islands that are not part of the copper oxide film.[16] The well-defined nanostructures seen in Figures 2e,f and 3e,f were not seen for these islands.[16] At large coverages of the oxide overlayer, separated domains of MgO and CuO_x coexisted and the film of copper oxide was in an amorphous state.[16]

Reaction of CH_4 with $MgO/CuO_x/Cu(111)$: AP-XPS Analysis. Figure 4 displays C 1s XPS spectra collected while exposing $CuO_x/Cu(111)$ surfaces precovered with 0.036 (left-side panel) and 0.11 ML (right-side panel) of MgO to different pressures of methane at 300 K. Neither plain $CuO_x/Cu(111)$ nor bare Cu(111) will dissociate methane at room temperature. In Figure 4, the three peaks near 286 eV come from gas phase methane.[14,15] At a low pressure of 10^{-6} Torr, a clear signal is seen around 284 eV that denotes the presence of CH_x (x = 2 or 3) fragments[20−22] on the surface produced by the partial dissociation of methane:

$$CH_{4,gas} \rightarrow {}^{*}CH_x + (4 - x){}^{*}H \tag{1}$$

Near 289 eV is seen a weak signal that points to the formation of a carbonate ($^{*}CO_3$):[20−22]

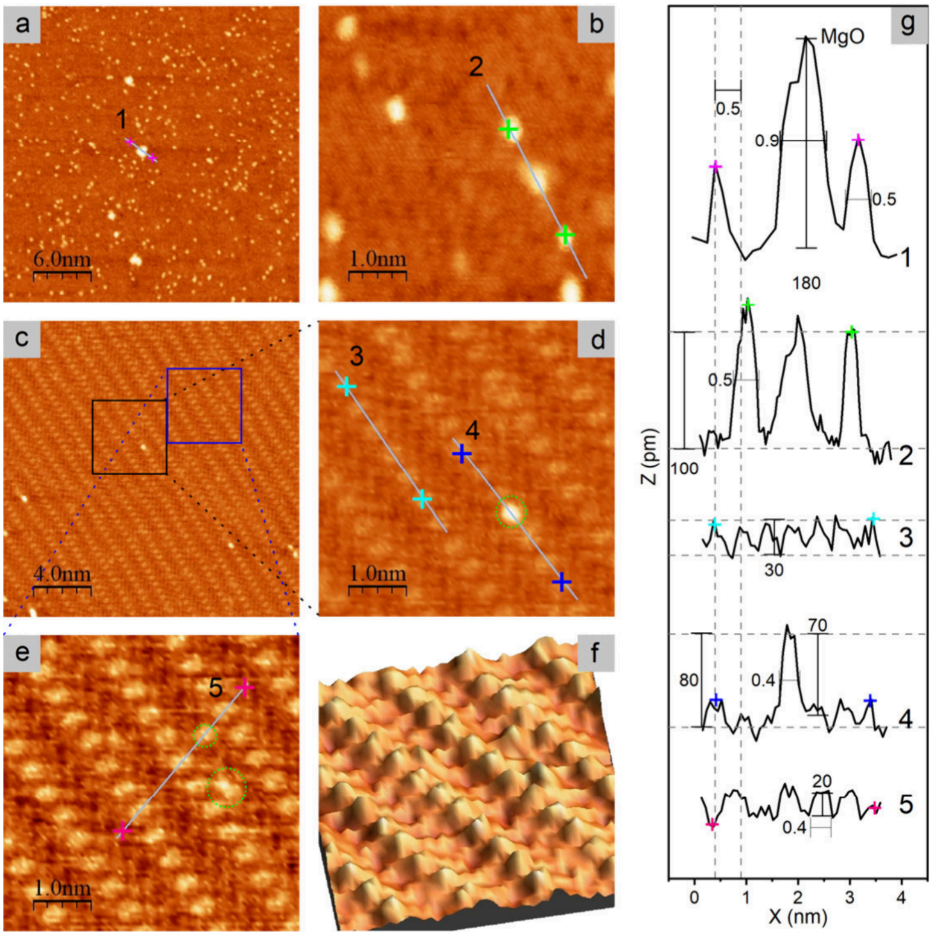

Figure 3. STM images of 0.1 ML of $MgO/CuO_x/Cu(111)$ surfaces. $Cu_2O/Cu(111)$ was prepared by exposing a pristine Cu(111) surface to O_2 (5×10^{-7} Torr) at 750 K for 20 min, and Mg was deposited on top of the surface at 300 K (a, b). In the final step, the $MgO/CuO_x/Cu(111)$ surface was exposed to O_2 (5×10^{-7} Torr) at 500 K (c, d, and e). (f) 3D representation of e. (g) Line profiles over various regions on b, d, and e. Nanostructures of MgO are shown inside a green circle in d, MgO embedded in a row of copper oxide, and e, MgO embedded in between rows of copper oxide. Imaging parameters: $I_t = -0.13$ nA, $V_s = -0.6$ V.

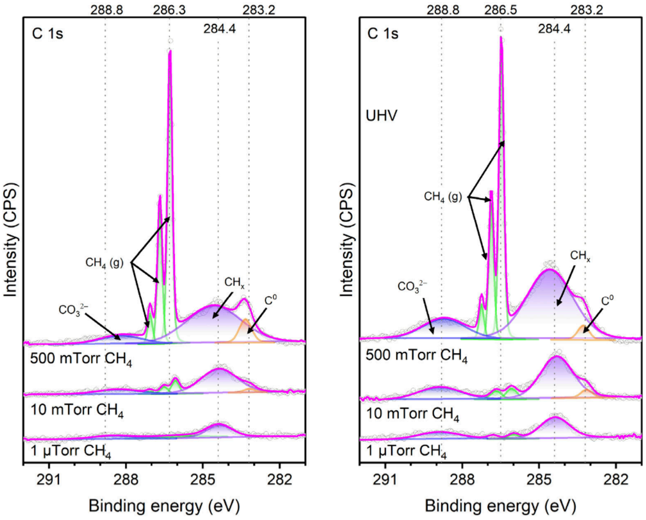

Figure 4. C 1s AP-XPS spectra collected while exposing 0.04 ML (left panel) and 0.11 ML (right panel) of MgO dispersed on Cu2O/Cu(111) to different pressures of CH_4 at 300 K. The $MgO/CuO_x/Cu(111)$ surfaces were prepared following the procedure shown in Figure 1 with the deposition of Mg on $Cu_2O/Cu(111)$ at 300 K and subsequent oxidation in O_2 at 500 K.

$$^{*}CH_x \rightarrow {}^{*}C + x{}^{*}H \tag{2}$$

$$^{*}C + 3O_{oxide} \rightarrow {}^{*}CO_3 \tag{3}$$

Evidence for the production of *C and $^*CO_3$ becomes clearer when the methane pressure is increased to 10 mTorr, but the peak for adsorbed CH_x fragments is always dominant. The ratio of coverage for the $^*C/^*CH_x$ species is larger for the surface with only 0.04 ML of MgO. The small clusters of MgO embedded in copper oxide (Figures 2 and 3) truly had special chemical properties.

Figure 5 displays sequential C 1s and O 1s AP-XPS spectra obtained during exposure of the 0.11 ML $MgO/CuO_x/Cu(111)$ surface to methane pressures from 1 μTorr to 500 mTorr at 300 K, followed by evacuation of the molecule and a final XPS scan. In the O 1s spectra, peaks at 529.5 and 528.9 eV, corresponding to O_L and O_{NL} atoms in copper oxide, are shifted (−0.4 eV) to lower binding energies compared with Figure 1. MgO peaks at 531.3 eV are consistent with previously reported data.[9,17,30] The peak for the O-bound copper decreased continuously when the surface was exposed to methane. The H adatoms produced by reactions 1 and 2 spilled onto the copper oxide and probably removed oxygen by the formation of water:

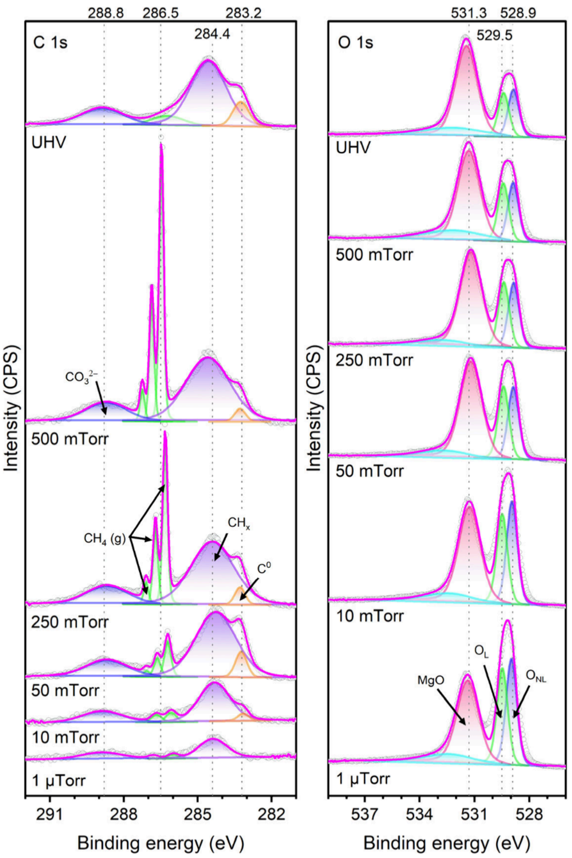

Figure 5. C and O 1s AP-XPS spectra collected while exposing a 0.11 ML MgO/CuO$_x$/Cu(111) surface to 1 μTorr to 500 mTorr of CH$_4$ at 300 K. Then, all CH$_4$ was evacuated, and the final XPS scan was taken. In a preliminary step, the surface was exposed to O$_2$ (1 × 10^{-6} Torr) at 500 K for 15 min; see Figure 1.

$$2^{*}\mathrm{H} + \mathrm{O}_{\mathrm{oxide}} \rightarrow \mathrm{H}_2\mathrm{O}_{\mathrm{gas}} \quad (4)$$

This is a process that is known to happen for the reduction of Cu$_2$O/Cu(111) with H$_2$ at room temperature.[22] Interestingly, the supported MgO nanostructures were not reduced, while pure copper oxide disappeared (Figures 5 and S2). This trend reflects differences in the thermochemical stability of MgO and copper oxides.[32] In previous studies examining the reaction of H$_2$ with MgO/Cu$_x$O/Cu(111) surfaces,[16] we found no signs for the reduction of MgO nanostructures or Mg−O−Cu interfaces at temperatures between 300 and 500 K. On the other hand, the pure copper oxide was reduced.[16] In Figure 5, we can see that the removal of copper-bound O is happening at the same time that CH$_x$, C, and CO$_3$ intermediates are being deposited on the surface. After gas evacuation, the MgO and *CH$_x$ groups are the dominant species.

Following the evacuation of all gases, the same MgO/CuO$_x$/Cu(111) surface was exposed again to 500 mTorr of the methane at 300 K and then heated to 500 at 100 K intervals (Figures 6 and S3). The peak features around 284 and 285 eV clearly changed. As the MgO/CuO$_x$/Cu(111) surface was heated, a signal appeared near 285 eV that can be assigned to C−C coupling and the formation of C$_2$H$_x$ groups.[33−35] The intensity of the carbonate features gradually decreased, probably as a consequence of surface decomposition. At 500 K, the O 1s peak at ∼531.4 eV could contain contributions from Mg−OH and some form of *CO species.[36,37] The AP-XPS results in Figures 4−6 show a very rich surface chemistry for methane on the MgO nanoparticles dispersed on CuO$_x$/Cu(111).The oxide nanostructures are far from being an inert system as bulk MgO is.[9] Previous studies have shown that corner sites in particles of MgO bind CO better than flat surfaces of the bulk oxide.[38] A similar phenomenon probably happens for methane adsorption. A hypothesis that is supported by the theoretical studies is described in the next section.

Reaction of CH$_4$ with MgO/CuO$_x$/Cu(111): DFT Studies. DFT calculations were carried out to gain an understanding of the methane dissociation process on the MgO/Cu$_2$O/Cu(111) surfaces. The STM images and line

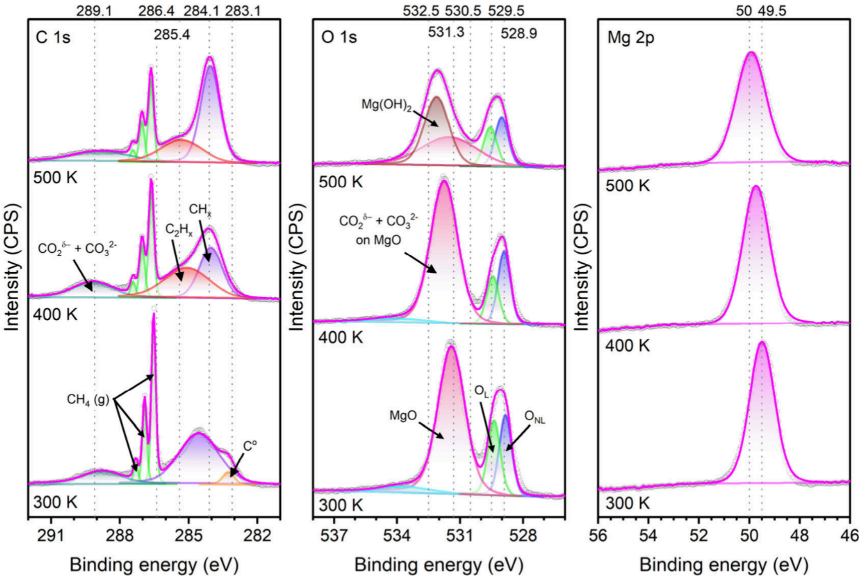

Figure 6. C 1s, O 1s, and Mg 2p AP-XPS spectra collected while exposing a 0.11 ML MgO/CuO$_x$/Cu(111) surface to 500 mTorr of CH$_4$ between 300 and 600 K. In a preliminary step, the surface was exposed to O$_2$ (1 × 10^{-6} Torr) at 500 K for 15 min (Figure 1) and then exposed to CH$_4$ at 300 (Figure 3).

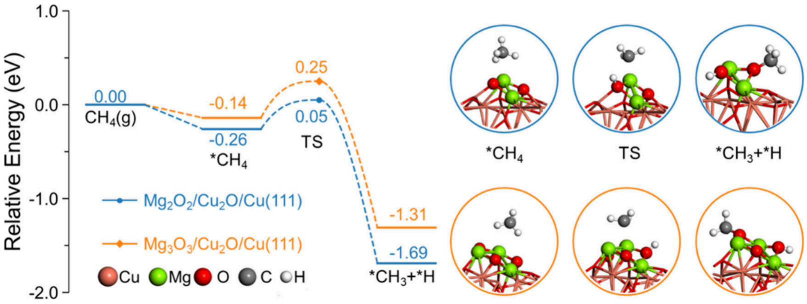

Figure 7. DFT-calculated potential energy diagram and DFT-optimized structures for CH_4 adsorption and dissociation on $Mg_2O_2/Cu_2O/Cu(111)$ and $Mg_3O_3/Cu_2O/Cu(111)$ surfaces. See Figures S6 and S7 for detailed top and side views.

profiles in Figures 2 and 3 indicate that the active nanostructures contain two or three units of MgO in contact with copper oxide, with sizes ranging from 0.3 to 0.4 nm. MgO size effects associated with methane activation were described using $Mg_3O_3/Cu_2O/Cu(111)$ and $Mg_2O_2/Cu_2O/Cu(111)$ models (0.27−0.38 nm in size for the MgO units; see structural details in Figure S4). Herein, $Mg_3O_3/Cu_2O/Cu(111)$ was reported previously as a selective catalyst for methane to methanol conversion.[18] The interaction of CH_4 with both surfaces was weak (Figures 7 and Figure S5), with $Mg_2O_2/Cu_2O/Cu(111)$ providing slightly stronger binding (adsorption energy: $E_{ads} = -0.26$ eV) than that on the $Mg_3O_3/Cu_2O/Cu(111)$ model ($E_{ads} = -0.14$ eV). A more significant promoting effect was observed for the first C−H bond dissociation on $Mg_2O_2/Cu_2O/Cu(111)$ (reaction energy: $\Delta E = -1.43$ eV, activation energy: $E_a = 0.31$ eV, Figure 7, Figure S6) compared to $Mg_3O_3/Cu_2O/Cu(111)$ ($\Delta E = -1.17$ eV, $E_a = 0.39$ eV, Figure 7,Figure S7). In this case, the smaller size of Mg_2O_2 helps to stabilize the dissociated $*CH_3$ fragment and thus lowers the activation barrier as compared to that of Mg_3O_3 (Figure 7). Nonetheless, the size effect is moderate. The final state on the supported Mg_2O_2 and Mg_3O_3 clusters involved $*CH_3$ and *H fragments bonded to low coordinated O sites of magnesium oxide, and both structures offered low enough activation barriers to enable the first hydrogen abstraction of CH_4 at room temperature, which is consistent with the XPS observations (Figure 4). Such exceptional activity for methane activation has not been observed previously for bulk MgO[9] and for several copper-based systems.[6,19−21,39] For example, an energy barrier of ~4.7 eV has been calculated with DFT for the dissociation of the first C−H bond of methane on MgO(100).[9] This energy barrier can be reduced to ~1.3 eV after doping the oxide with Li.[9] An electron transfer from the alkali metal to the oxide facilitates C−H bond breaking.[1,9,14] As we will discuss below, an electron transfer from copper to MgO could be enhancing the reactivity of the oxide overlayer[15,18] and help with the dissociation of methane. Differences in the Madelung potential when going from a bulk system to nanoparticles also could help to enhance the reactivity of our MgO systems.[40] In addition, the MgO nanostructures in Figures 2, 3, and 7 have Mg and O sites with a low coordination number, which are not seen in a flat MgO(100) surface, and help in the binding and dissociation of the alkane (Figures 7 and S5−S7).

Resistance of the supported MgO clusters to reduction (Figure 7) was seen for the active O sites. These sites bind *H strongly enough (adsorption energy, $E_{ads} = -1.44$ eV) to hinder further reduction and oxygen vacancy (O_v) formation on the MgO clusters (formation energy of O_v, $E_f = 3.74$ eV) according to our DFT calculations. Instead, the *H species in Figure 7 could migrate to O centers bound to Cu, which are less active to anchor *H (E_{ads}(*H) = −0.64 eV, −0.67 eV at non-lattice fcc and hcp O sites) and allow subsequent reduction of the Cu_2O layer as seen in previous DFT calculations and AP-XPS experiments.[22]

Coupling of CH_4 to C_2H_6 and C_2H_4 on $MgO/CuO_x/Cu(111)$: Catalytic Studies. As mentioned in the introduction, over a MgO-based catalyst, activated methane has the potential to be transformed into ethane or ethylene.[9−11] The AP-XPS results in Figure 6 suggest the formation of C_2H_x groups at 400 and 500 K. As a case study, we decided to investigate methane coupling on $MgO/CuO_x/Cu(111)$ with 0.1 ML of MgO (Figure 8). C_2H_6, C_2H_4, and H_2 were detected as products of methane coupling. The results in Figure 8 were obtained in a batch reactor with an initial pressure of 5 Torr of methane at 500 K. By far, ethane was the main C_2 hydrocarbon produced, and the amount of H_2 generated was close to that expected for a mixture of C_2H_6/C_2H_4 as reaction products. The MgO nanostructures in contact with copper operate at a much lower temperature than those used for methane coupling on bulk MgO (>700 K).[9−11,14] The $MgO/CuO_x/Cu(111)$ surface shows catalytic activity at a temperature that is comparable to that found for a Pt/SiO_2 catalyst (520 K),[41] but our system is stable with time.

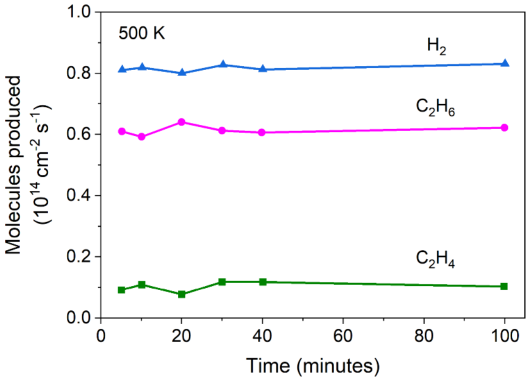

Figure 8. Production of ethane, ethylene, and hydrogen through methane coupling on a 0.1 ML $MgO/CuO_x/Cu(111)$ surface exposed to 5 Torr of CH_4 at 500 K.

Figures S8 and S9 show the O and C 1s XPS spectra collected after performing the $CH_4 \rightarrow C_2H_6$, C_2H_4 reactions on the $MgO_x/CuO_x/Cu(111)$ catalyst. In the O 1s region, there were distinct features that point to the coexistence of MgO and CuO_x on the Cu(111) substrate, in good agreement with the O 1s AP-XPS data displayed in Figure 6 for a MgO/

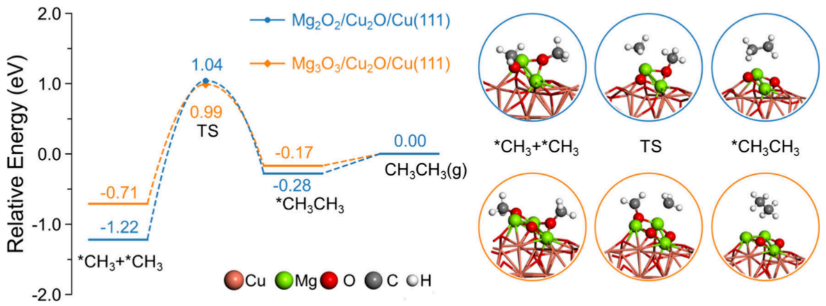

Figure 9. DFT-calculated potential energy diagram and DFT-optimized structures for surface $^*CH_3$ coupling to CH_3CH_3 on $Mg_2O_2/Cu_2O/Cu(111)$ and $Mg_3O_3/Cu_2O/Cu(111)$ models. See Figure S11 and Figure S12 for detailed top and side views.

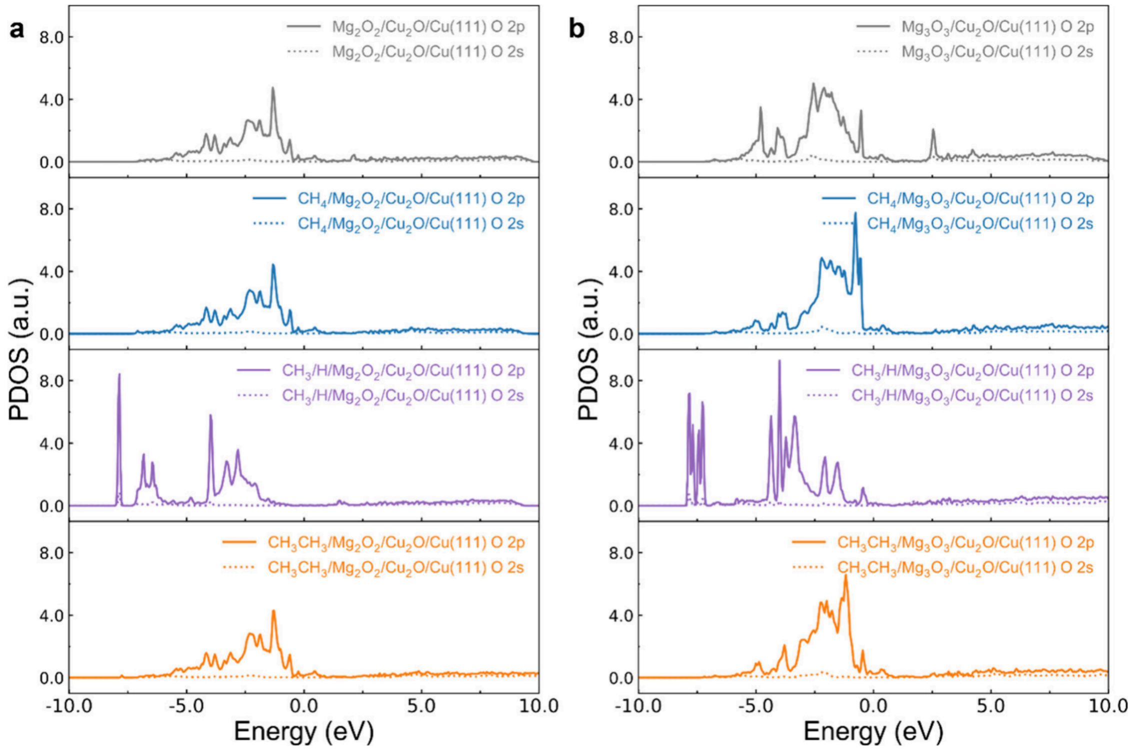

Figure 10. Partial density of states (PDOS) for levels with O 2p and 2s character of a Mg_2O_2 cluster in $Mg_2O_2/Cu_2O/Cu(111)$ (panel a) and a Mg_3O_3 cluster in $Mg_3O_3/Cu_2O/Cu(111)$ (panel b). From top to bottom, the figure includes results for each bare surface (black traces), with $^*CH_4$ adsorption (blue traces), with $^*CH_3$+$^*H$ adsorption (purple traces), and with $^*CH_3CH_3$ adsorption (orange traces).

$CuO_x/Cu(111)$ surface exposed to methane at 400 and 500 K. The well-ordered surface morphology seen in Figure 3 did not survive under the reaction conditions. The pure copper oxide was removed, and only the CuO_x that was associated with MgO remained. Essentially, the active phase of the catalysts contained composite nanostructures of Mg−O−Cu. The coverage of C present on the 0.1 ML $MgO/CuO_x/Cu(111)$ catalyst was negligible (Figure S9). The system in Figure 8 did not undergo deactivation due to carbon deposition or coke formation as seen for bulk MgO[7,9] or a Pt/SiO_2 catalyst.[41] When the MgO coverage was increased in the $MgO_x/CuO_x/Cu(111)$ systems, the amount of C deposited increased (Figure S9) and there was a significant drop in catalytic activity (Figure S10). However, even with a partially blocked surface by C, the $MgO_x/CuO_x/Cu(111)$ catalysts were always much more active than bulk MgO.[7,9] Clusters and nanostructures of MgO in contact with $CuO_x/Cu(111)$ (Figures 3 and 4, and ref 16) displayed a substantial ability to enable the $CH_4 \rightarrow C_2H_6$, C_2H_4 conversions.

Coupling of CH_3 to C_2H_6 on $MgO/Cu_2O/Cu(111)$: DFT Studies. The results in Figure 7 for the activation of methane on $Mg_2O_2/Cu_2O/Cu(111)$ and $Mg_3O_3/Cu_2O/Cu(111)$ surfaces can be used as the starting point for the generation of ethane. Compared to CH_4 dissociation, the C−C coupling of dissociated $^*CH_3$ species to produce $^*CH_3CH_3$ is a more difficult process,[7,9−11] and here we just focus on qualitative aspects of the reaction, which can be effectively hindered by stabilization of the $^*CH_3$ groups on the catalyst surface. Indeed, due to the strong binding of $^*CH_3$ species on $Mg_2O_2/Cu_2O/Cu(111)$, the C−C coupling is very difficult both thermodynamically and kinetically (ΔE = 0.94 eV, E_a = 2.26 eV, Figure 9, Figure S11). As a comparison, this process is significantly favored by decreases in reaction and activation energies when increasing the size of the MgO cluster from Mg_2O_2 to Mg_3O_3 (ΔE = 0.54 eV, E_a = 1.70 eV, Figure 9, Figure S12). Upon the formation of $^*CH_3CH_3$ species, the removal is facile on the $Mg_2O_2/Cu_2O/Cu(111)$ (E_{des} = −0.28 eV) and $Mg_3O_3/Cu_2O/Cu(111)$ models (E_{des} = −0.17 eV)

https://doi.org/10.1021/acsnano.4c10811
ACS Nano 2024, 18, 28371−28381

(Figure S13). That is, the production of C_2H_6 that was measured experimentally can strongly depend on the size of the supported MgO cluster (Figure 9).

In principle, the optimal conversion of CH_4 to C_2H_6 requires a moderate binding to $*CH_3$, strong enough to facilitate a C−H bond scission in CH_4, but weak enough to enable C−C coupling with the generated $*CH_3$.[2,7,9] For MgO/Cu_2O/Cu(111), the energetics of the two steps (i.e., C−H bond cleavage and C−C bond formation) display different dependence on the size of the MgO cluster, with the former being less sensitive than the latter. Specifically, a small MgO cluster, i.e., Mg_2O_2, binds $*CH_3$ strongly to enhance C−H activation in methane but significantly hinders the C−C coupling to yield C_2H_6, while a larger MgO cluster, i.e., Mg_3O_3, still enables CH_4 dissociation but destabilizes the binding of $*CH_3$ to facilitate its coupling to C_2H_6. The difference in dependence on the size of MgO between C−H bond scission and C−C coupling is attributed to the selective bond-tuning by varying the MgO size. For the reaction intermediates, more tuning on binding energy to the open-shell $*CH_3$ is observed than seen for the closed-shell $*CH_4$ and $*C_2H_6$ (Figures 7 and 9) molecules. This is reflected in significant changes in the 2p position according to the calculated density of states (Figure 10). The selectively stabilized $*CH_3$ on Mg_2O_2/Cu_2O/Cu(111) is associated with higher lying O 2p states in Mg_2O_2 than in Mg_3O_3, resulting in a more significant down-shift and thus stronger binding on interaction with $*CH_3$ (Figure 10).

In terms of the transition states, the dissociation of CH_4 is featured with an early transition state, resembling the configuration and energetics of the initial state (Figure 7). Therefore, the weakened $*CH_3$ binding on moving from Mg_2O_2 to Mg_3O_3 does not effectively increase the activation energy (0.31 vs 0.39 eV). On the other hand, the C−C coupling adopts a late transition state, where the energy differences in the final and transition states of Mg_2O_2 and Mg_3O_3 are small (Figure 9). As a result, the stability of the initial states, $*CH_3$, dominates and determines the activation barrier (2.26 vs 1.7 eV). But, on both MgO clusters, the energy barrier for C−C coupling is much smaller than on bulk MgO.[9] In qualitative terms, the DFT results demonstrate size-dependent C−H bond breaking and C−C bond formation of methane over MgO clusters. Accordingly, as the size of the MgO cluster increases toward bulk MgO, binding to CH_4 and $*CH_3$ weakens to the point that it is extremely difficult to dissociate methane and subsequent C−C bond formation,[9] and, at the same time, at high temperatures there is a problem with the formation of a $MgOC_x$ compound as a side reaction during the alkane activation.[1,2,7,9]

Previous works examining the behavior of MgO overlayers on metal substrates have reported a charge transfer from the metal to the oxide that can enhance the chemical reactivity of MgO.[13,15] Note that in the model systems of Figures 7 and 9, the Cu_2O/Cu(111) substrate also helps stabilizing $*CH_3$ and thus tuning C−H bond scission and C−C coupling. Specifically, there is a charge transfer from the Cu ion that binds to the active O sites neighbor to $*CH_3$, which is again more significant for Mg_2O_2 as compared to Mg_3O_3 (Figure S14). For both systems, a redistribution of electrons occurs in the Mg−O−Cu units once the H_3C-CH_3 bond is formed.

CONCLUSIONS

AP-XPS studies, supported by STM observations, indicate that MgO nanostructures (0.2−0.5 nm in width and 0.4−0.6 Å in height) embedded on Cu_2O/Cu(111) surfaces can activate methane at room temperature. These nanostructures primarily dissociate methane into CH_x (x = 2 or 3) and H adatoms, with only a small amount of methane fully decomposing to yield C adatoms, which can further react with surface oxygen to form CO_x species. Unlike bulk MgO, MgO nanostructures on CuO_x/Cu(111) display a large reactivity, enabling C−C coupling to yield ethane and ethylene at a relatively low temperature of 500 K without deactivation from carbon or coke deposition.

DFT studies reinforce these experimental findings, pointing to a highly exothermic $CH_{4,gas} \rightarrow *CH_3 + *H$ process on the MgO/Cu_2O/Cu(111) surfaces. Methane activation is facilitated by electron transfer from copper to MgO and the presence of Mg and O atoms with a low coordination number in the oxide nanostructures. Smaller Mg_2O_2 clusters provide stronger binding and lower activation barriers for C−H bond dissociation compared to larger Mg_3O_3 clusters. While Mg_2O_2 enhances initial methane activation, Mg_3O_3 promotes subsequent C−C coupling to form ethane due to weaker $*CH_3$ binding.

Catalytic studies in a batch reactor confirmed that methane coupling over MgO/CuO_x/Cu(111) catalysts primarily produces ethane at 500 K, a significantly lower temperature than that required for bulk MgO catalysts (>700 K), with minimal carbon deposition. This performance is comparable to that of a Pt/SiO_2 catalyst but without the deactivation issues associated with carbon deposition, ensuring stable catalytic activity. These findings emphasize the importance of the size when optimizing the catalytic performance of MgO nanostructures for selective methane conversion.

METHODS

Ambient-Pressure X-ray Photoelectron Spectroscopy. All AP-XPS investigations were conducted at beamline 23-ID-2 (IOS) of the National Synchrotron Light Source II (NSLS-II) at Brookhaven National Laboratory (BNL), following established procedures for this specific beamline and end station.[42] The Cu (111) crystal (SPL EU.01) was cleaned by successive cycles of Ar^+ ion sputtering (2×10^{-5} Torr Ar gas, 1 keV, 20 min) at 300 K, followed by UHV annealing at 900 K for 10 min, repeated until carbon and oxygen traces in the XPS C 1s and O 1s regions were eliminated. Subsequently, a thin copper oxide film was generated on the Cu (111) surface by exposure to 1×10^{-6} Torr of O_2 at 600 K for 10 min, with subsequent cooling to 300 K in the same environment. MgO nanostructures were synthesized through physical vapor deposition,[16] involving the deposition of Mg onto the Cu_2O/Cu (111) surface using a commercial metal evaporator (CreaTec low-temperature effusion cell) at ambient temperature. The varying Mg coverages on the copper oxide substrate were determined by analyzing the surface atomic ratios of Mg and Cu using their respective 2p peaks in XPS spectra.[16] To facilitate both CH_4 activation and its coupling studies, the Mg/CuO_x/Cu (111) surface underwent oxidation by heating at 500 K for 15 min in the presence of 1×10^{-6} Torr of O_2 in the background.

AP-XPS spectra were obtained under CH_4 pressures spanning from 1 μTorr to 500 mTorr (equivalent to 1.33×10^{-6} to 0.666 mbar). To investigate the CH_4 reaction on the Mg/Cu_xO/Cu (111) surface, CH_4 gas was initially introduced at 1 μTorr at 300 K, gradually increasing the pressure to 500 mTorr, followed by stepwise temperature increments (100 K intervals) to 700 K. XPS spectra were collected for the C 1s, O 1s, Cu 2p, and Mg 2p regions at each step. Photon energies of 250, 450, 680, and 1050 eV were employed for exciting the Mg 2p, C 1s, O 1s, and Cu 2p regions, respectively, ensuring uniform probing depths. Data collection utilized a step size of 0.05 eV, with an overall energy resolution of approximately 0.2 eV.

https://doi.org/10.1021/acsnano.4c10811
ACS Nano 2024, 18, 28371−28381

The binding energy scale was aligned to the valence band Fermi edge at each photon energy, maintaining a consistent value (74.9 ± 0.1 eV) for the bulk $3p_{3/2}$ peak of Cu. After binding-energy positions were calibrated with the valence band spectra, a Shirley-type background was applied to Mg 2p, O 1s, and C 1s spectra.

Scanning Tunneling Microscopy. The STM images were collected in an ultrahigh-vacuum (UHV) system with a base pressure of 1×10^{-10} Torr, which housed a variable-temperature scanning tunneling microscope (Omicron VT-STM).[16] A single-side-polished Cu (111) single crystal (MaTeck GmbH) was meticulously cleaned through cycles of Ar^+ ion sputtering (Scienta Omicron, 2 kV, 15 min) and subsequent annealing (750 K, 10 min) within the UHV preparation chamber ($P_{base} < 1 \times 10^{-10}$ Torr). The Cu_xO thin film was formed via annealing at 750 K for 20 min, followed by cooling to room temperature over 10 min, maintaining a background pressure of 5×10^{-7} Torr O_2.[3] Verification of sample cleanliness and the formation of a Cu_xO "29" structure[4] were conducted through STM measurements. The growth of MgO nanostructures on pristine copper oxide took place at 300 K by utilizing the same metal evaporator employed in the AP-XPS studies. STM imaging was performed at room temperature using a sharpened Pt−Ir tip (Unisoku Japan) in constant current mode, with typical tunneling conditions specified as V_s for sample bias and I_t for tunneling current, often set at $I_t = -0.13$ nA and $V_s = -0.6$ V. MgO coverage was achieved through estimation of the area of protruding features on the CuO_x/Cu(111) surface, while the determination of MgO particle size in data analysis involved averaging across all particles in the images rather than relying on a single value.

Catalytic Tests. The catalytic activity of the $MgO/Cu_2O/Cu(111)$ surfaces for the coupling of methane was investigated employing an instrument that combines a UHV chamber for surface characterization (equipped with XPS, Auger electron spectroscopy, low-energy electron diffraction, and ion scattering spectroscopy) and a small reaction cell in a batch configuration.[19−21] The $MgO/Cu_2O/Cu(111)$ samples were prepared following the methodology shown in Figure 1. They were moved to the batch reactor at 300 K and exposed to a reaction feed of 5 Torr of methane (99.999% purity). The production of C_2H_6, C_2H_4, and H_2 was followed using a combination of mass spectroscopy and gas chromatography.[19−21] The kinetic studies were done always under a low conversion of methane (<5%). Steady state was reached after 2−3 min of reaction, and under pure methane no signs of catalyst deactivation were found in a period of 2 h when the measurements ended.

Density Functional Theory Calculations. Spin-polarized DFT[43] implemented in Vienna *ab initio* simulation package (VASP)[44] was used to perform all the calculations. A 400 eV kinetic energy cutoff and the projector-augmented wave method (PAW)[45] together with the GGA exchange−correlation functional plus the PBE functional[46] were employed. Monkhorst−Pack[47] meshes with 3 × 3 × 1 were used to sample the Brillouin zone for all the surface calculations, while gamma points were employed for all gas-phase species. The nudged elastic band method (NEB)[48] for each elementary reaction intermediates was performed to derive the transition states. The criteria for total energies and forces on all atoms were set as 10^{-5} eV and 0.02 eV $Å^{-1}$ for convergence, respectively. Gaussian smearing with a width of 0.05 eV was used to improve the convergence. The dispersion forces were not considered here due to the overestimation of the strong interactions, according to our previous studies.[18−22] $MgO/Cu_2O/Cu(111)$ catalyst was simulated with a three-layer 4 × 4 Cu(111) surface and one monolayer of Cu_xO ($x \approx 1.13$) with M_3O_3 or M_2O_2 clusters deposited on top (Figure S4). The Mg (2p, 3s), Cu (3p, 3d, 4s), C (2s, 2p), O (2s, 2p), and H (1s) electrons were treated as valence states, while the remaining electrons were kept frozen as core states. The Hubbard-like U term[49] was considered to address Cu 3d electrons for the Cu_xO surface (U_{eff} = 5.2),[35] in which the Coulomb U and exchange J parameters were combined into a single parameter, $U_{eff} = U - J$. During DFT optimizations, the bottom two layers were fixed while the rest were allowed to relax with adsorbates.

ASSOCIATED CONTENT

Supporting Information

The Supporting Information is available free of charge at https://pubs.acs.org/doi/10.1021/acsnano.4c10811.

> XPS and Auger spectra for the characterization of $MgO/CuO_x/Cu(111)$ surfaces; additional results of catalytic tests and postreaction characterization of the catalyst surface with XPS; discussion of surface models and additional theoretical results (PDF)

AUTHOR INFORMATION

Corresponding Author

José A. Rodriguez − *Chemistry Division, Brookhaven National Laboratory, Upton, New York 11973, United States; Department of Chemistry, Stony Brook University, Stony Brook, New York 11794, United States;* orcid.org/0000-0002-5680-4214; Phone: 631-344-2246; Email: rodrigez@bnl.gov

Authors

Arephin Islam − *Chemistry Division, Brookhaven National Laboratory, Upton, New York 11973, United States;* orcid.org/0000-0001-8528-859X

Erwei Huang − *Chemistry Division, Brookhaven National Laboratory, Upton, New York 11973, United States;* orcid.org/0000-0003-2690-3788

Yi Tian − *Department of Chemistry, Stony Brook University, Stony Brook, New York 11794, United States*

Pedro J. Ramírez − *Facultad de Ciencias, Universidad Central de Venezuela, Caracas 1020-A, Venezuela; Zoneca-CENEX, R&D Laboratories, 64770 Monterrey, México*

Kasala Prabhakar Reddy − *Chemistry Division, Brookhaven National Laboratory, Upton, New York 11973, United States*

Hojoon Lim − *National Synchrotron Light Source II, Brookhaven National Laboratory, Upton, New York 11973, United States;* orcid.org/0000-0001-5106-511X

Nathaniel White − *Department of Chemistry, University of Michigan, Ann Arbor, Michigan 48109, United States;* orcid.org/0000-0003-4174-1297

Adrian Hunt − *National Synchrotron Light Source II, Brookhaven National Laboratory, Upton, New York 11973, United States;* orcid.org/0000-0002-5283-9647

Iradwikanari Waluyo − *National Synchrotron Light Source II, Brookhaven National Laboratory, Upton, New York 11973, United States;* orcid.org/0000-0002-4046-9722

Ping Liu − *Chemistry Division, Brookhaven National Laboratory, Upton, New York 11973, United States; Department of Chemistry, Stony Brook University, Stony Brook, New York 11794, United States;* orcid.org/0000-0001-8363-070X

Complete contact information is available at: https://pubs.acs.org/10.1021/acsnano.4c10811

Notes

The authors declare no competing financial interest.

ACKNOWLEDGMENTS

The research done at the Chemistry Division of Brookhaven National Laboratory was supported by the U.S. Department of Energy, Office of Science, Office of Basic Energy Sciences, Chemical Sciences, Geosciences, and Biosciences Division, Catalysis Science Program (Grant No. DE-SC0012704). PJR is grateful to Zoneca-CENEX for an internal grant that made possible part of this research. This research used resources of the 23-ID-2 (IOS) beamline of the National Synchrotron Light Source II, a U.S. Department of Energy (DOE) Office of Science User Facility operated for the DOE Office of Science by Brookhaven National Laboratory under Contract No. DE-SC0012704.

REFERENCES

(1) Meng, X.; Cui, X.; Rajan, N. P.; Yu, L.; Deng, D.; Bao, X. Direct methane conversion under mild condition by thermo-, electro-, or photocatalysis. *Chem.* **2019**, *5*, 2296−2325.

(2) McFarland, E. Unconventional chemistry for unconventional natural gas. *Science* **2012**, *338*, 340.

(3) Istadi, I., Thermodynamic Analysis of Synthesis Gas and Higher Hydrocarbons Production from Methane. In *Syngas: Production, Applications and Environmental Impact*; Nova Science Publishers: New York, 2012.

(4) Hussien, A. G. S.; Polychronopoulou, K. A Review on the Different Aspects and Challenges of the Dry Reforming of Methane (DRM) Reaction. *Nanomaterials* **2022**, *12*, 3400.

(5) Navarro, R. M.; Peña, M. A.; Fierro, J. L. G. Hydrogen production reactions from carbon feedstocks: Fossil fuels and biomass. *Chem. Rev.* **2007**, *107*, 3952−3991.

(6) Rodriguez, J. A.; Rui, N.; Zhang, F.; Senanayake, S. D. In-Situ Studies of Methane Activation Using Synchrotron-based Techniques: Guiding the Conversion of C-H bonds. *ACS Catal.* **2022**, *12*, 5470−5488.

(7) Schwach, P.; Frandsen, W.; Willinger, M.-G.; Schlögl, R.; Trunschke, A. Structure sensitivity of the oxidative activation of methane over MgO model catalysts: I. Kinetic study. *J. Catal.* **2015**, *329*, 560−573.

(8) Zuo, Z.; Liu, S.; Wang, Z.; Liu, C.; Huang, W.; Huang, J.; Liu, P. Dry Reforming of Methane on Single-Site Ni/MgO Catalysts: Importance of Site Confinement. *ACS Catal.* **2018**, *8*, 9321−9835.

(9) Pal, R. S.; Rana, S.; Sadhu, S.; Khan, T. S.; Poddar, M. K.; Singha, R. K.; Sarkar, S.; Sharma, R.; Bal, R. Highly active and selective Li/MgO catalysts for methane transformation to C_2 hydrocarbons: Experimental and DFT study. *Energy Adv.* **2023**, *2*, 189−197.

(10) Grant, J. T.; Venegas, J. M.; McDermott, W. P.; Hermans, I. Aerobic Oxidation of Light Alkanes over Solid Metal Oxide Catalysts. *Chem. Rev.* **2018**, *118*, 2769−2815.

(11) Peil, K. P.; Goodwin, J.; Marcelin, G. Surface Phenomena during the Oxidative Coupling of Methane over Li/MgO. *J. Catal.* **1991**, *131*, 143−155.

(12) Barman, S.; Kundu, A. K.; Menon, K. S. R. Growth and coverage dependent electronic structure of MgO on Ag(001). *Surf. Sci.* **2018**, *677*, 60−67.

(13) Pacchioni, G.; Freund, H. Electron Transfer at Oxide Surfaces. The MgO Paradigm: from Defects to Ultrathin Films. *Chem. Rev.* **2013**, *113*, 4035−4072.

(14) Luo, L.; Jin, Y.; Pan, H.; Zheng, X.; Wu, L.; You, R.; Huang, W. E. Distribution of Li in Li-doped MgO Catalysts for Oxidative Coupling of Methane. *J. Catal.* **2017**, *346*, 57−61.

(15) Pacchioni, G.; Freund, H.-J. Controlling the charge state of supported nanoparticles in catalysis: lessons from model systems. *Chem. Soc. Rev.* **2018**, *47*, 8474−8502.

(16) Prabhakar Reddy, K.; Islam, A.; Tian, Y.; Lim, H.; Kim, J.; Kim, D.; Hunt, A.; Waluyo, I.; Rodriguez, J. A. MgO Nanostructures on Cu(111): Understanding Size- and Morphology-Dependent CO_2 Binding and Hydrogenation. *J. Phys. Chem. C* **2024**, *128*, 7149−7158.

(17) Pacchioni, G. Physisorbed and chemisorbed CO_2 at surface and step sites of the MgO(100) surface. *Surf. Sci.* **1993**, *281*, 207−219.

(18) Huang, E.; Liu, P. Screening of Cu-Based Catalysts for Selective Methane to Methanol Conversion. *J. Phys. Chem. C* **2024**, *128*, 7876−7883.

(19) Huang, E.; Orozco, I.; Ramírez, P. J.; Liu, Z.; Zhang, F.; Mahapatra, M.; Nemšák, S.; Senanayake, S. D.; Rodriguez, J. A.; Liu, P. Selective Methane Oxidation to Methanol on $ZnO/Cu_2O/Cu(111)$ Catalysts: Multiple Site-Dependent Behaviors. *J. Am. Chem. Soc.* **2021**, *143*, 19018−19032.

(20) Huang, E.; Rui, N.; Rosales, R.; Liu, P.; Rodriguez, J. A. Activation and Conversion of Methane to Syngas over $ZrO_{2/}Cu(111)$ Catalysts near Room Temperature. *J. Am. Chem. Soc.* **2023**, *145*, 8326−8331.

(21) Liu, Z.; Huang, E.; Orozco, I.; Liao, W.; Palomino, R. M.; Rui, N.; Duchoň, T.; Nemšák, S.; Grinter, D. C.; Mahapatra, M.; Liu, P.; Rodriguez, J. A.; Senanayake, S. D. Water-promoted interfacial pathways in methane oxidation to methanol on a CeO_2/Cu_2O catalyst. *Science* **2020**, *368*, 513−517.

(22) Mehar, V.; Huang, E.; Shi, R.; Rui, N.; Rosales, R.; Waluyo, I.; Hunt, A.; Liu, P.; Rodriguez, J. A. Microscopic Investigation of H_2 Reduced $CuO_x/Cu(111)$ and $ZnO/CuO_x/$ Cu(111) Inverse Catalysts: STM, AP-XPS, and DFT Studies. *ACS Catal.* **2023**, *13*, 9857−9870.

(23) Kahk, J. M.; Lischner, J. Core electron binding energies of adsorbates on Cu(111) from first-principles calculations. *Phys. Chem. Chem. Phys.* **2018**, *20*, 30403−30411.

(24) Lee, Y. J.; Ly, T. T.; Lee, T.; Palotás, K.; Jeong, S. Y.; Kim, J.; Soon, A. Completing the Picture of Initial Oxidation on Copper. *Appl. Surf. Sci.* **2021**, *562*, No. 150148.

(25) Cabailh, G.; Lazzari, R.; Cruguel, H.; Jupille, J.; Savio, L.; Smerieri, M.; Orzelli, A.; Vattuone, L.; Rocca, M. Stoichiometry-Dependent Chemical Activity of Supported MgO(100) Films. *J. Phys. Chem. A* **2011**, *115*, 7161−7168.

(26) Savio, L.; Celasco, E.; Vatuonne, L.; Rocca, M. Enhanced Reactivity at Metal−Oxide Interface: Water Interaction with MgO Ultrathin Films. *J. Phys. Chem. B* **2004**, *108*, 7771−7778.

(27) Yang, F.; Choi, Y.; Liu, P.; Hrbek, J.; Rodriguez, J. A. Autocatalytic Reduction of a $Cu_2O/Cu(111)$ Surface by CO: STM, XPS, and DFT Studies. *J. Phys. Chem. C* **2010**, *114*, 17042−17050.

(28) Yang, F.; Choi, Y.; Liu, P.; Stacchiola, D.; Hrbek, J.; Rodriguez, J. A. Identification of 5−7 Defects in a Copper Oxide Surface. *J. Am. Chem. Soc.* **2011**, *133*, 11474−11477.

(29) Jensen, F.; Besenbacher, F.; Lægsgaard, E.; Stensgaard, I. Oxidation of Cu(111): two new oxygen induced reconstructions. *Surf. Sci.* **1991**, *259*, L774−L780.

(30) Besenbacher, F.; Norskov, J. K. Oxygen-Chemisorption on Metal-Surfaces - General Trends for Cu Ni and Ag. *Prog. Surf. Sci.* **1993**, *44*, 5−66.

(31) Chen, J. L.; Zhu, J. H.; Chen, J. L.; Zhu, J. H. A query on the Mg 2p binding energy of MgO. *Res. Chem. Intermed.* **2019**, *45*, 947−950.

(32) *Lange's Handbook of Chemistry*, 13th ed.; Dean, J. E., Ed.; McGraw-Hill: New York, 1985; pp 9−21 (the $\Delta H_f°$ of CuO and Cu_2O are −37.6 and −40.3 kcal/mol, respectively) and page 9−34 (the $\Delta H_f°$ of MgO is −144 kcal/mol).

(33) Freiberger, E. M.; Düll, F.; Wichmann, C.; Bauer, U.; Steinrück, H.-P.; Papp, C. A High-resolution X-ray Photoelectron Spectroscopy Study on the Adsorption and Reaction of Ethylene on Rh(111). *Chem. Phys. Lett.* **2022**, *797*, No. 139595.

(34) Isaacs, M. A.; Davies-Jones, J.; Davies, P. R.; Guan, S.; Lee, R.; Morgan, D. J.; Palgrave, R. Advanced XPS characterization: XPS-based multi-technique analyses for comprehensive understanding of functional materials. *Mater. Chem. Front.* **2021**, *5*, 7931−7963.

(35) Xu, L.; Wu, Z.; Wang, H.; Shi, J.; Li, Z.; Huang, W. Adsorption and Surface Reactions of C_2H_2 and C_2H_4 on Co(0001). *Surf. Sci. Technol.* **2023**, *1*, 5−13.

(36) Simonovis, J. P.; Zhang, H.; Rui, N.; Hunt, A.; Orozco, I.; Liu, P.; Senanayake, S. D.; Rodriguez, J. A.; Waluyo, I. Investigating the Elusive Nature of Atomic O from CO_2 Dissociation on Pd(111): The Role of Surface Hydrogen. *J. Phys. Chem. C* **2022**, *126*, 7870−7879.

(37) Kaichev, V. V.; Prosvirin, I. P.; Bukhtiyarov, V. I.; Unterhalt, H.; Rupprechter, G.; Freund, H.-J. High-Pressure Studies of CO

Adsorption on Pd(111) by X-ray Photoelectron Spectroscopy and Sum-Frequency Generation. *J. Phys. Chem. B* **2003**, *107*, 3522−3527.

(38) Spoto, G.; Gribov, E. N.; Ricchiardi, G.; Damin, A.; Scarano, D.; Bordiga, S.; Lamberti, C.; Zecchina, A. Carbon Monoxide MgO from Dispersed Solids to Single Crystals: A Review and New Advances, *Progress. Surf. Sci.* **2004**, *76*, 71−146.

(39) Zuo, Z.; Ramírez, P. J.; Sennayake, S. D.; Liu, P.; Rodriguez, J. A. Low-Temperature Conversion of Methane to Methanol on CeO_x/Cu_2O Catalysts: Water Controlled Activation of the C−H Bond. *J. Am. Chem. Soc.* **2016**, *138*, 13810−13813.

(40) Stefanovich, E. V.; Truong, T.; N. Correlation between the Madelung Field and the Reactivity of the MgO Low-coordinated Surface Sites. *J. Chem. Phys.* **1995**, *102*, 5071−5076.

(41) Belgued, M.; Pareja, P.; Amariglio, A.; Amariglio, H. Conversion of Methane into Higher Hydrocarbons on Platinum. *Nature* **1991**, *352*, 789−790.

(42) Waluyo, I.; Hunt, A. Ambient Pressure X-Ray Photoelectron Spectroscopy at the IOS (23-ID-2) Beamline at the National Synchrotron Light Source II. *Synchrotron Radiat. News* **2022**, *35*, 31−38.

(43) Hohenberg, P.; Kohn, W. Inhomogeneous electron gas. *Phys. Rev.* **1964**, *136*, B864−B871. Kohn, W.; Sham, L. J. Self-consistent equations including exchange and correlation effects. *Phys. Rev.* **1965**, *140*, A1133−A1138.

(44) Kresse, G.; Furthmuller, J. Efficient iterative schemes for ab initio total-energy calculations using a plane-wave basis set. *Phys. Rev. B* **1996**, *54*, 11169−11186.

(45) Perdew, J. P.; Burke, K.; Ernzerhof, M. Generalized gradient approximation made simple. *Phys. Rev. Lett.* **1996**, *77*, 3865−3868.

(46) Blochl, P. E. Projector augmented-wave method. *Phys. Rev. B* **1994**, *50*, 17953−17979. Kresse, G.; Joubert, D. From ultrasoft pseudopotentials to the projector augmented-wave method. *Phys. Rev. B* **1999**, *59*, 1758−1775.

(47) Monkhorst, H. J.; Pack, J. D. Special points for Brillouin-zone integrations. *Phys. Rev. B* **1976**, *13*, 5188−5192.

(48) Henkelman, G.; Jonsson, H. Improved tangent estimate in the nudged elastic band method for finding minimum energy paths and saddle points. *J. Chem. Phys.* **2000**, *113*, 9978−9985.

(49) Dudarev, S. L.; Botton, G. A.; Savrasov, S. Y.; Humphreys, C. J.; Sutton, A. P. Electron-energy-loss spectra and the structural stability of nickel oxide: An LSDA+U study. *Phys. Rev. B* **1998**, *57*, 1505−1509.